Imaging of the Surface Resistance of an SRF Cavity by Low-Temperature Laser Scanning Microscopy

Gianluigi Ciovati, Steven M. Anlage, and Alexander V. Gurevich

***Abstract*—Temperature mapping of the outer surface of a superconducting radio-frequency cavity is a technique that is often used to identify lossy areas on the cavity surface. In this contribution, we present 2-D images of the superconducting state surface resistance R_s of the inner surface of a superconducting radio-frequency (SRF) cavity obtained by low-temperature laser scanning microscopy. This technique, which is applied for the first time to study lossy regions in an operating SRF cavity, allows identifying "hotspots" with about one order of magnitude better spatial resolution ($\sim$2 mm) than by thermometry. The R_s-resolution is of the order of 1 $\mu\Omega$ at 3.3 GHz. Surface resistance maps with different laser power and optical images of the cavity surface are discussed in this contribution. It is also shown that the thermal gradient on the niobium surface created by the laser beam can move some of the hotspots, which are identified as locations of trapped bundle of fluxoids. The prospects for this microscope to identify defects that limit the performance of SRF cavities will also be discussed.**

***Index Terms*—Laser scanning microscopy, niobium, superconducting accelerator cavities, surface resistance.**

I. Introduction

TEMPERATURE mapping of the *outer* surface of superconducting radio-frequency (SRF) cavities immersed in either superfluid or subcooled liquid He has been the only technique to measure non-uniform RF losses occurring on the *inner* surface, where the superconducting current flows within the penetration depth ($\sim$40 nm in Nb) [2], [3]. Some of the challenges include the presence of ultra-high vacuum and strong electromagnetic fields inside the cavity, along with the needs to avoid particulate contamination of the inner surface and the fairly large surface areas involved, compared to coupon samples (the surface area of a single-cell 1.3 GHz cavity is $\sim$1 m^2). Low temperature laser scanning microscopy (LTLSM) is a well-known technique to characterize thin-film microwave resonators made of high-temperature superconducting materials [4], [5] and involves point-by-point raster scanning of a focused laser beam onto the surface of the sample, then measuring the photoresponse induced by the interaction of the light with the superconductor, as a function of the laser spot position (x, y).

The same technique can be applied to map the surface resistance, R_s, of a bulk cavity surface and an experimental apparatus was built at Jefferson Lab for such purpose. The apparatus is briefly described in Section II and in [1] in greater details. Hotspots have been located by conventional temperature mapping and 2D images of R_s at these locations have been obtained by LTLSM for different parameters, such as laser power and modulation frequency. These results are shown in Section III.

Magnetic flux due to residual Earth's magnetic field inside the cryostat or to thermoelectric currents can be trapped in the niobium during cool-down below the critical temperature, T_c. Trapped fluxoids are one among many possible causes of enhanced RF dissipation leading to hotspots [6]. The availability of a high-power laser on the LTLSM setup allows creation of a thermal gradient of intensity sufficient to de-pin fluxoids. Temperature maps taken before and after laser sweeping will be shown in Section IV.

II. Experimental

A. Experimental Setup

The LTLSM is assembled on a vertical test stand, about 230 cm high and 81 cm in diameter, to be inserted in the cryostat. The optical components are mounted on an optical table bolted to the test stand's top plate. The optical components include: a 10 W, 532 nm, continuous wave laser, a $\lambda/2$ waveplate and a polarizer cube to adjust the laser power, a negative lens on a translational stage followed by a positive lens with long focal length to focus the beam at the cavity location, mirrors to keep the beam within the test stand perimeter and to bend the beam downward towards the cavity. By adjusting the position of the negative lens with respect to that of the fixed positive lens, the diameter of the laser beam at the cavity location can be adjusted between $\sim$0.9–3.0 mm.

The laser beam travels inside a vacuum pipe, below the top plate, which is connected to a mirrors' chamber, also under vacuum (total pressure of about 2×10^{-7} mbar), which houses two mini-stepper motors holding two flat laser mirrors positioned in such a way to allow x-y scanning of the beam.

The SRF cavity is bolted at the bottom of the mirrors' chamber and a UV-grade fused silica optical window separates the cavity volume from the mirrors' chamber's volume, to reduce particulate contamination of the cavity surface.

Manuscript received October 3, 2012; accepted December 6, 2012. Date of publication December 10, 2012; date of current version February 19, 2013. This manuscript has been authored by Jefferson Science Associates, LLC, under US DOE Contract DE-PS02-09ER09-05. The work at the University of Maryland was supported by DOE Grant DESC0004950 and ONR/AppEl Task D10, through Grant N000140911190. Additional support for this work was provided by the US Government Presidential Early Career Award for Scientists and Engineers.

G. Ciovati is with Thomas Jefferson National Accelerator Facility, Newport News, VA 23606 USA (e-mail: gciovati@jlab.org).

S. M. Anlage is with the Department of Physics, Center for Nanophysics and Advanced Materials, University of Maryland, College Park, MD 20742 USA (e-mail: anlage@umd.edu).

A. V. Gurevich is with the Department of Physics, Old Dominion University, Norfolk, VA 23529 USA (e-mail: agurevic@odu.edu).

Color versions of one or more of the figures in this paper are available online at http://ieeexplore.ieee.org.

Digital Object Identifier 10.1109/TASC.2012.2233253

The SRF cavity consists of a 1.3 GHz half-cell with a flat, ∼21 cm diameter plate at the bottom. The aperture of the cavity cut-off tube allows the laser beam reaching a radius of ∼40 mm from the center of the plate, corresponding to an angle of incidence of about ±7° from the direction normal to the plate. The cavity was built from ingot Nb with nominal residual resistivity ratio of ∼200. The cavity is excited in the TE_{011} mode resonating at ∼3.3 GHz. Operating in the TE_{011} mode makes the cavity less susceptible to "extrinsic" phenomena such as field emission and multipacting.

An array of 128 resistor-temperature-devices (RTDs), distributed in concentric circular patterns with increasing diameter, is attached to the bottom cavity plate to obtain temperature maps of the flat plate's outer surface during RF test at 2.0 K. The distance between each RTD and its neighbors is ∼12–20 mm. Further details on all the components of the microscope can be found in [1]. The outer surface of the cavity and the thermometry system are fully immersed in the liquid He bath inside the cryostat.

B. Experimental Procedure

The quality factor of the cavity, Q_0, at 2.0 K is $\sim 10^9 - 10^{10}$ and a phase-locked loop is used to maintain the RF system locked to the cavity frequency with a certain fixed incident power. The laser power, $P_{\rm L}$, is modulated, between 0% and 100%, at a frequency $f_{\rm M}$ using a TTL signal from a function generator, which also provides the reference signal to a lock-in amplifier. The change in the transmitted power from the cavity due to the laser amplitude changing between 0% and 100% is measured with the lock-in amplifier. The change in transmitted power is proportional to the change in power dissipated on the cavity surface. Photons from the laser are absorbed by Cooper pairs and quasi-particles in the superconductor, increasing the temperature and, in turn, the quasi-particle density and therefore the local $R_{\rm s}$. The fraction of laser power, $P_{\rm L}$, absorbed by the Nb plate is ∼21% [1]. Assuming that the local magnetic field is temperature independent and that $R_{\rm s}(T_{\rm f}) \gg R_{\rm s}(T_{\rm i})$, where $T_{\rm f}$ and $T_{\rm i}$ are the local surface temperatures with laser on and off, respectively, the local $R_{\rm s}$ can be calculated from measured quantities as follows [1]:

$$R_s(x,y,f_M) \cong \frac{\pi}{\sqrt{2}} \frac{\delta V_{rms}(x,y,f_M)}{V_0\left[1-\left(\frac{Q_L}{Q_{ext1}}+\frac{Q_L}{Q_{ext2}}\right)\right]} \cdot \frac{P_{c0}}{H^2(x,y)\pi r_L^2} \tag{1}$$

where V_0 is a DC voltage proportional to the transmitted power when the laser is off, $\delta V_{\rm rms}$ is the rms voltage measured by the lock-in amplifier while pulsing the laser, H is the local magnetic field amplitude, $r_{\rm L}$ is the laser beam radius, $Q_{\rm L}$ is the cavity loaded Q, $P_{\rm c0}$ is the RF power dissipated on the cavity surface with laser off, $Q_{\rm ext1}$ and $Q_{\rm ext2}$ are the external Q-values of the input and transmitted probe, respectively. The (x, y) dependence reflects the dependence on the laser beam position on the cavity plate, while the $f_{\rm M}$ dependence is related to $T_{\rm f}$, as lower $T_{\rm f}$ are obtained with higher $f_{\rm M}$, for the same laser power.

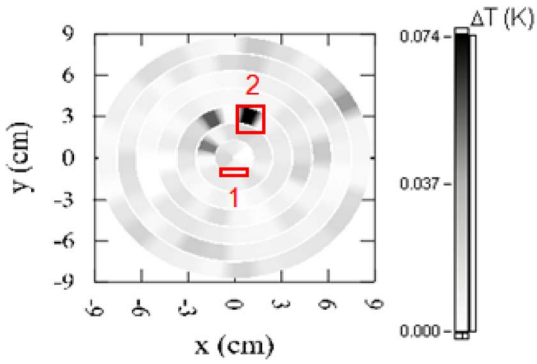

Fig. 1. Temperature map of the bottom cavity plate at 2.0 K and $B_{\rm p} = 13$ mT, showing a temperature rise ΔT of up to ∼75 mK in three spots. Two-dimensional images of $R_{\rm s}$ at locations "1" and "2" obtained by LTLSM are shown in Fig. 2.

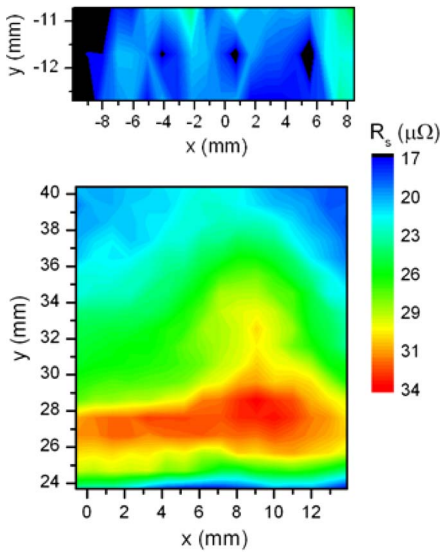

Fig. 2. Two-dimensional images of the surface resistance at locations "1" (top) and "2" (bottom), shown in Fig. 1. A ∼ 2 mm × 14 mm region at location "2" with $R_{\rm s}$ higher by about a factor of two than that of location "1" was obtained, causing the higher temperature rise on the outer surface, shown in Fig. 1.

III. LTLSM Results

Fig. 1 shows a temperature map of the cavity plate measured at a peak surface magnetic field, $B_{\rm p}$, of ∼13 mT and He bath temperature of 2.0 K and Fig. 2 shows 2D images of $R_{\rm s}$ obtained by LTLSM at the locations marked in Fig. 1, showing a comparison between a "coldspot" and a "hotspot" location. The cavity Q_0-value is $\sim 2.2 \times 10^9$. A laser power of ∼4.4 W, $r_{\rm L} \sim 0.44$ mm and $f_{\rm M} = 10$ Hz were used for these measurements. The thermal "hotspot" corresponds to a region of enhanced surface resistance.

Fig. 3 shows the temperature map of the bottom cavity plate during another RF test at 2.0 K, $B_{\rm p} = 14$ mT. 2D images of the local $R_{\rm s}$, over the area shown in the red box in Fig. 3 are shown in Fig. 4 for different laser power, ranging between ∼250 mW and ∼4.4 W. For all measurements, $r_{\rm L} \sim 0.44$ mm and $f_{\rm M} = 1$ Hz. $T_{\rm f}$ estimated by a finite-element thermal analysis of the 3 mm thick Nb plate with 2.0 K liquid He on one side and a Gaussian heat flux distribution on the other side, representing the incident laser beam, is shown in

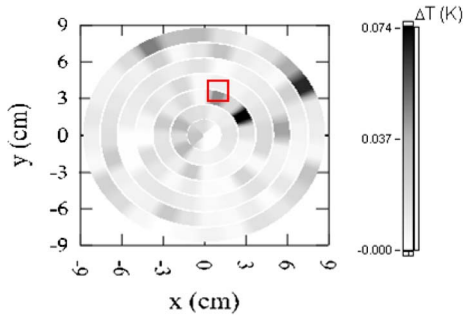

Fig. 3. Temperature map of the bottom cavity plate at 2.0 K and $Bp = 14$ mT, showing a temperature rise ΔT of up to ~75 mK in two spots. Two-dimensional images of R_s at the location marked with the red box obtained by LTLSM are shown in Fig. 4.

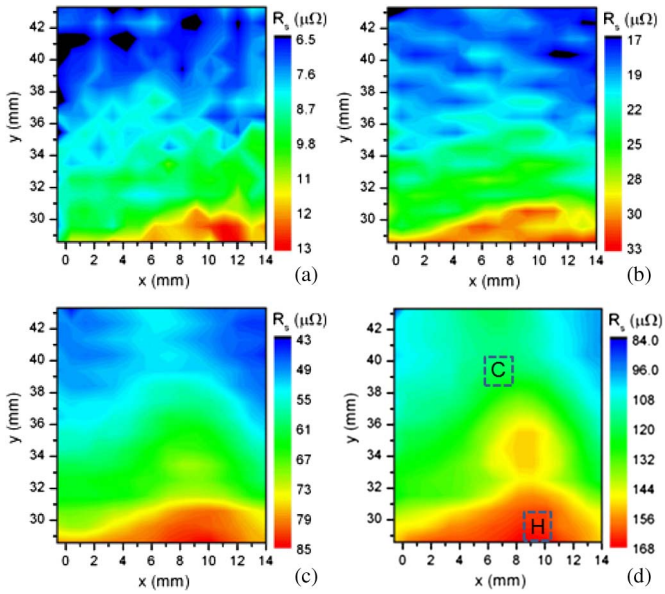

Fig. 4. Two-dimensional images of the surface resistance at the locations shown in Fig. 3 for different laser power values: (a) ~250 mW, (b) ~1.7 W, (c) ~2.76 W, and (d) ~4.4 W. The measurements were done with the same laser beam radius ($r_L \cong 0.44$ mm) and modulation frequency ($f_M = 1$ Hz). The average values of R_s as a function of temperature in regions "C" and "H" are shown in Fig. 5(d).

Table I for the laser power values used to obtain the images shown in Fig. 4. The Bardeen-Cooper-Schrieffer (BCS) surface resistance, R_{BCS}, at 3.3 GHz was calculated using the code developed by Halbritter [7] for the temperature values shown in Table I and the following Nb material parameters: $T_c = 9.25$ K, energy gap at 0 K divided by the product of the Boltzmann constant times T_c, $\Delta/kT_c = 1.76$, BCS coherence length, $\xi = 31$ nm, London penetration depth, $\lambda_L = 42$ nm and normal electrons' mean free path, $l = 10$ nm. The calculated values of RBCS are listed in Table I and they are in good agreement with the lowest R_s-values shown in Fig. 4 for each laser power setting. The residual resistance, R_{res}, obtained from a fit of $R_s(T) = R_{BCS}(T) + R_{res}$ between 4.2 K and 2.0 K was ~130 nΩ, negligible compare to $R_{BCS}(T_f)$.

By calculating the point-by-point ratio of R_s at different laser power levels it is possible to obtain maps showing non-uniformities in the temperature dependence of R_s. Such maps are shown in Fig. 5(a)–(c). The average ratios are $R_s(\sim 6\ \text{K})/R_s(\sim 4.5\ \text{K}) = 2.6 \pm 0.3$, $R_s(\sim 7.5\ \text{K})/R_s(\sim 6\ \text{K}) = 2.7 \pm 0.2$, $R_s(\sim 8.4\ \text{K})/R_s(\sim 7.5\ \text{K}) = 2.2 \pm 0.1$. These values are consistent with the ratios of R_{BCS} values calculated using the material parameters mentioned earlier. The average R_s-values from regions labeled "C" and "H" in Fig. 4(d) are shown in Fig. 5(d) as a function of temperature. A fit of the data with the BCS theory numerical program indicate that region "H" has the weakest superconductivity, within the area delimited by the red box in Fig. 3: $\Delta/kT_c = 1.49 \pm 0.17$ in region "H", $\Delta/kT_c = 1.67 \pm 0.12$ in region "C". The mean free path is about 5 nm in both cases. The other material parameters (T_c, λ_L, ξ) were not used to fit the data and their values were those mentioned earlier. The results indicating low values of l and Δ/kT_c could be explained by the presence of normal-conducting sub-oxides or hydrides.

TABLE I
LASER POWER, PEAK INNER SURFACE TEMPERATURE DUE TO LASER HEATING AND BCS SURFACE RESISTANCE

P_L (W)	T_f (K)	R_{BCS} (3.3 GHz, T_f) (μΩ)
0.25	~4.5	~5.3
1.7	~6.0	~15
2.76	~7.5	~42
4.4	~8.4	~110

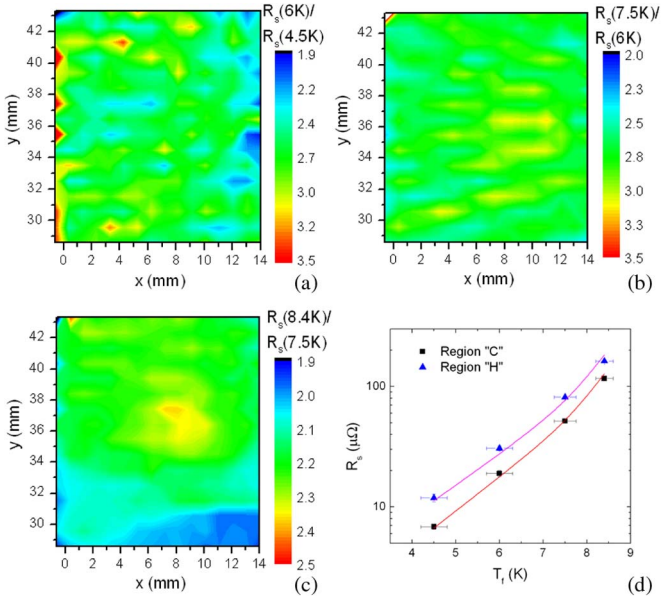

Fig. 5. (a)–(c) Two-dimensional maps showing the ratios of R_s-values from Fig. 4 at different laser power levels and therefore different T_f-values. (d) Average R_s-values in regions "H" and "C" shown in Fig. 4(d) along with fits to the BCS theory (solid lines).

Higher laser power increases the signal-to-noise ratio but also the perturbation of the local superconducting state. For the same laser power, increasing f_M decreases T_f as the temperature rise does not reach the steady state (low frequency) value. This is shown, for example, in Fig. 6 where ΔT measured on the outer cavity surface is plotted as a function of time for a laser excitation with $P_L \cong 4.4$ W, $r_L \cong 0.44$ mm and $f_M = 1$ Hz and 10 Hz. The "dip" at $\Delta T \cong 0.4$ K is attributed to changes in the heat transfer coefficient at the Nb/He II interface as the heat flux increases above the value which causes film boiling conditions to occur at the Nb/Ne II interface.

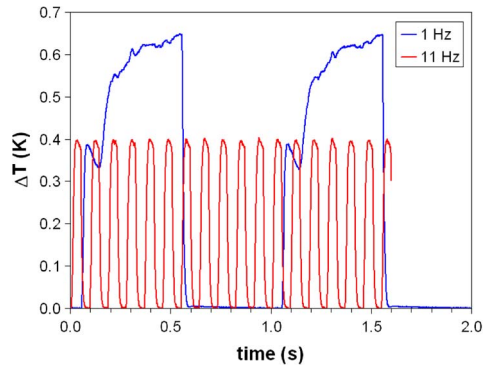

Fig. 6. Temperature rise as a function of time measured by a RTD on the outer cavity surface due to the laser beam ($r_{\rm L} \cong 0.44$ mm, $P_{\rm L} \cong 4.4$ W) heating the inner surface for different modulation frequencies. The ΔT measured by the RTD should be divided by the RTD efficiency (estimated to be $\sim$20%) to obtain the effective temperature rise.

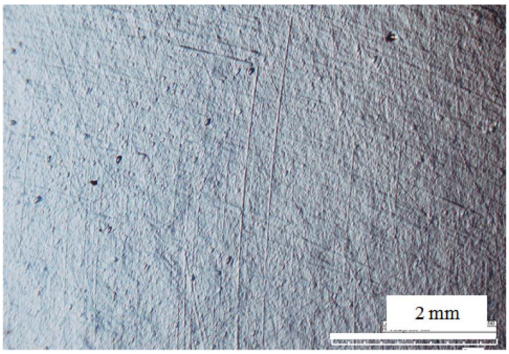

Fig. 7. Optical microscopy image (50 times magnification) of an area at the inner surface of the cavity plate ($x \cong 0-6$ mm, $y \cong 26-30$ mm), which includes the high-$R_{\rm s}$ region shown in Fig. 4.

The $R_{\rm s}$-sensitivity increases with increasing amplitude of the local magnetic field, it is limited by the noise in $\delta V_{\rm rms}$ and it is estimated to be $\sim$1 $\mu\Omega$ at 3.3 GHz and at the $B_{\rm p}$ location.

After a series of tests, the flat plate was cut from the cavity by wire electro-discharge machining, locations with high $R_{\rm s}$ identified by LTLSM were marked on the plate and examined with a high resolution microscope. Geometrical defects of $\sim 50-100$ μm size have sometimes been found at quench locations at the inner surface of multi-cell cavities. Nevertheless, none of the high-$R_{\rm s}$ locations in this particular cavity showed an outstanding geometrical feature. Fig. 7 shows the optical microscopy image covering the area at $x \cong 0-6$ mm, $y \cong 26-30$ mm. A few pits of $\sim$100 μm size are visible in this region, but they were also commonly found at other locations of the cavity plate.

IV. Laser Sweeping of Hotspots

The number and intensity of hotspots is found to increase with increasing surface field. The origin of such hotspots is still unclear. Possibilities include lossy oxides/suboxides, formation of niobium hydrides and premature local quench due to geometric field enhancement. Losses due to fluxoids pinned in the Nb cavity during cool-down across $T_{\rm c}$ in a residual magnetic field could also produce hotspots at high RF fields. The LTLSM setup provides a convenient way to test for the presence of pinned fluxoids at hotspot locations because, unlike geometric features, or interstitial impurities, they can be moved by a thermal gradient [6] while the cavity is superconducting. The thermal force acting on a fluxoid is given by [8]:

$$f_T = -S\nabla T \tag{2}$$

where $S = \Phi_0|\partial H_{\rm c1}/\partial T|$ is the fluxoid transport entropy per unit vortex length, Φ_0 is the magnetic flux quantum, and $H_{\rm c1}$ is the lower critical magnetic field. If the thermal force is greater than the pinning force, fluxoids will move in the opposite direction of the applied thermal gradient. The direction that the fluxoids will move to depends critically on their direction with respect to the inner surface, where the thermal gradient is established. Pinning is fairly weak in Nb and, assuming $J_{\rm c} \cong 10^7$ A/m^2, it was estimated that a temperature gradient of $\sim$1.7 K/mm at $T = 2.0$ K should be sufficient to de-pin fluxoids and such temperature gradient can be easily exceeded at the inner surface with the available laser power. Similar manipulations of trapped magnetic flux had been already done in the past on Nb-Pb Josephson junctions [9] and YBCO films [10], [11] using electron beams or lasers.

The following procedure was adopted to evaluate the effect of laser sweeping of hotspots while the cavity is immersed in superfluid He at 2.0 K:

- A baseline RF test of the cavity is performed by measuring $Q_0(B_{\rm p})$ up to the highest achievable field. Temperature maps are taken at each $B_{\rm p}$-value.
- RF power is turned off, the laser is turned on, directed to some selected hotspot locations and swept around each of those locations. RTDs on the outer cavity surface are used to confirm the laser beam position.
- The laser is turned off, RF power is turned back on and a new $Q_0(B_{\rm p})$ measurement, along with temperature mapping, is done after laser heating.

In the following, we discuss, as an example, results obtained from one such series of tests. Fig. 8 shows a temperature map at $\sim$82 mT taken during the baseline RF test, during the RF test after horizontal laser sweep of hotspots and during RF test after additional hotspots laser sweeping following a spiral trajectory. The laser beam parameters were $r_{\rm L} \cong 0.44$ mm and $P_{\rm L} \cong 4.4$ W in both cases. Horizontal laser sweeps were repeated to cover an area of $\sim 16 \times 16$ mm^2 centered on each hotspot. The speed of the laser beam was $\sim$17 mm/s. For the second laser heating, an Archimedean spiral trajectory originating at the hotspots and with a maximum radius of 12 mm, 1 mm increment, $\sim$1.5 mm/s speed was tried. The baseline RF test was limited by multipacting-induced quench at $\sim$100 mT. The Q_0 at the quench field was $\sim 3.2 \times 10^9$. No significant changes in the $Q_0(B_{\rm p})$ curve were observed after laser heating.

The temperature rise at $\sim$75 mT as a function of location measured during the baseline test and tests after laser heating is shown in details in Fig. 9 for RTDs located along ring No. 2 and ring No. 3 (Ring No. 1 is the closest to the center of the plate). Horizontal sweeps were done at the following angular positions [shown in Fig. 8(a)]: $\theta = 75°$, 225° and 255° on ring 2; $\theta = 34°$, 124°, 169° and 259° on ring 3. Spiral sweeps were done at $\theta = 75°$, 255° and 340° on ring 2 and at $\theta = 169°$ and 259° on ring 3 [the locations are shown in Fig. 8(b)]. Changes

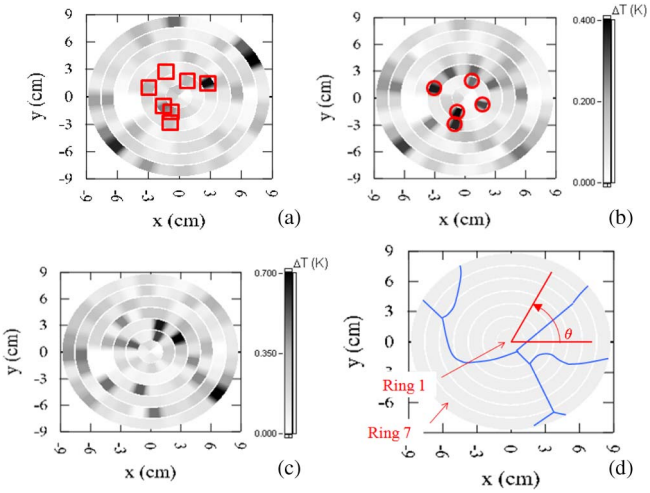

Fig. 8. Temperature map at 2.0 K, ∼82 mT measured during baseline RF test (a) and after laser heating of hotspots with horizontal (b) and spiral trajectories (c). The approximate locations of grain boundaries are shown as blue lines in (d). The red squares in (a) indicate the locations of the horizontal sweeps done after the baseline test. The red circles in (b) show the locations of the spiral sweeps done after the second test.

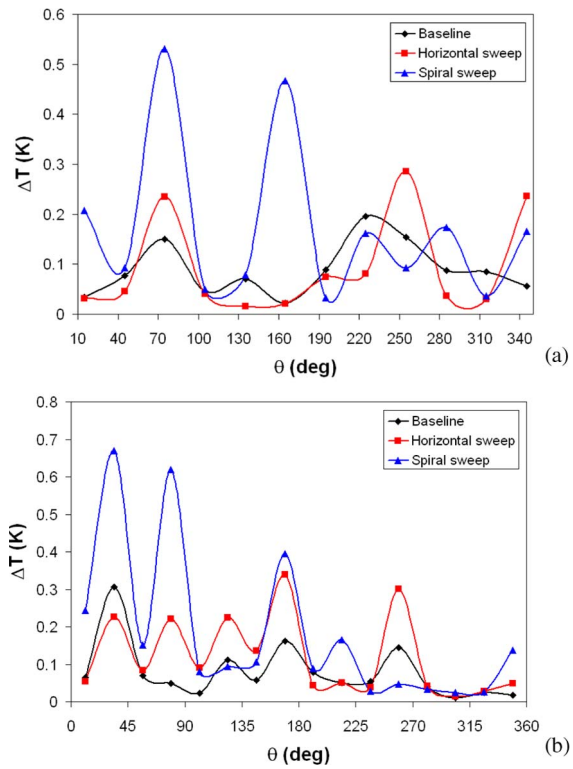

Fig. 9. Temperature rise at ∼75 mT along rings No. 2 (a) and No. 3 (b) during the baseline RF test and during RF tests after laser sweeping with horizontal or spiral trajectories of some of the hotspots. The ΔT measured by the RTDs should be divided by the RTD efficiency (estimated to be ∼20%) to obtain the effective temperature rise.

in hotspot locations after laser heating were clearly observed. This behavior was observed in several other series of tests. It should also be noted that the laser is kept on as the beam is moved to the different locations where the local horizontal or spiral sweeps were done. Therefore, the movement of fluxoids which might have been pinned at other locations along the path followed by the laser beam is also a possibility.

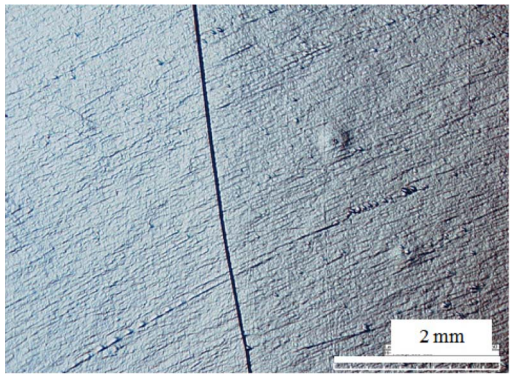

Fig. 10. Optical microscopy image (50 times magnification) of an area at the inner surface of the cavity plate ($x \cong -21$ to -15 mm, $y \cong -20.3$ to -15.7 mm) centered on $\theta = 225°$ on ring 2 showing the presence of a grain boundary.

Optical microscopy showed the presence of a grain boundary at $\theta = 225°$ on ring 2 (shown in Fig. 10) and at $\theta = 259°$ on ring 3 which can certainly be preferred locations to trap fluxoids. Further results on changes of thermal maps by laser sweeping will be presented and discussed in a separate publication.

V. Summary and Conclusion

Measurements of the local surface resistance of the inner surface of a niobium SRF cavity have been accomplished for the first time by LTLSM. It was shown that hotspots at low RF field measured by thermometry on the outer cavity surface correspond to regions of enhanced surface resistance by as much as a factor of ∼2 compared to "coldspot" areas. R_s of a "coldspot" is consistent with R_{BCS} at the estimated inner surface temperature. It was found that hotspots regions extend over several mm^2. Optical microscopy of hotspot regions did not reveal any unusual topological feature down to a size of ∼10 μm. For a better understanding of additional losses due to sharp edges, "controlled" defects could be made on the cavity surface and analyzed with the low-temperature laser scanning microscope.

As the region of the cavity perturbed by the laser is a small fraction of the total surface, a high quality factor $(Q_0 > 10^9)$ of the cavity is necessary for good R_s-resolution. Higher signal-to-noise ratio can be achieved by increased laser power or lower modulation frequency, both increasing the peak temperature of the inner surface. As a drawback, T_f-values which are several degrees higher than the bath temperature make a theoretical calculation of the local R_s more difficult, as the high-power laser introduces a large perturbation of the superconducting state.

Laser sweeping of hotspots occurring at "medium" RF fields (∼80 mT) was attempted in order to investigate whether pinned fluxoids might be present. Changes of temperature maps after *in situ* laser sweeping do confirm this possibility.

Using the microscope to measure R_s of SRF elliptical cavities operating in the TM_{010} mode used to accelerate the beam in a particle accelerator is fairly challenging. A schematic for a possible setup is shown in Fig. 11: a small, low-loss dielectric wafer could be inserted in the beam tube of the cavity, through a thin dielectric rod connected to a motion-controlled vacuum

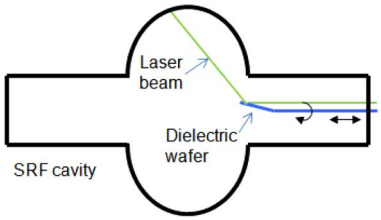

Fig. 11. Schematic of a possible setup to perform LTLSM of the inner surface of an SRF elliptical cavity operating in the TM_{010} mode.

feedthrough. A laser beam entering the cavity on the same side of the dielectric rod will be reflected by the wafer toward the equator region of the cavity, where high surface magnetic field is located.

Further insights on the origin of enhanced RF losses in SRF cavities by the LTLSM technique could be obtained by designing a test cavity where the surface magnetic field is concentrated in a small area accessible by the laser beam and such that the this high B-field region could be demounted from the rest of the cavity for surface analytical investigation and dedicated surface treatments.

ACKNOWLEDGMENT

G. C. would like to thank O. Trofimova of The College of William & Mary for helping with the optical microscopy and P. Kneisel of JLab for many useful discussions.

REFERENCES

[1] G. Ciovati *et al.*, "Low temperature laser scanning microscopy of a superconducting radio-frequency cavity," *Rev. Sci. Instrum.*, vol. 83, p. 034704, 2012.

[2] R. Romijn, W. Weingarten, and H. Piel, "Calibration of the scanning thermometer resistor system for a superconducting accelerating cavity," *IEEE Trans. Magn.*, vol. MAG-19, no. 3, pp. 1318–1321, 1983.

[3] J. Knobloch, H. Muller, and H. Padamsee, "Design of a high speed, high resolution thermometry system for 1.5 GHz superconducting radio frequency cavities," *Rev. Sci. Instrum.*, vol. 65, pp. 3521–3528, 1994.

[4] A. P. Zhuravel, A. G. Sivakov, O. G. Turutanov, A. N. Omelyanchouk, S. M. Anlage, and A. V. Ustinov, "Laser scanning microscopy of HTS films and devices," *Low Temp. Phys.*, vol. 32, no. 6, pp. 592–607, 2006.

[5] A. P. Zhuravel, S. M. Anlage, S. K. Remillard, A. V. Lukashenko, and A. V. Ustinov, "Effect of $LaAlO_3$ twin-domain topology on local dc and microwave properties of cuprate films," *J. Appl. Phys.*, vol. 108, p. 033920, 2010.

[6] A. Gurevich and G. Ciovati, "Dynamics of vortex penetration, jumpwise instabilities, and nonlinear surface resistance of type-II superconductors in strong rf fields," *Phys. Rev. B.*, vol. 77, p. 104501, 2008.

[7] J. Halbritter, FORTRAN Program for the Computation of the Surface Impedance of Superconductors, KFK-Extern 3/70-6, Karlsruhe, Germany, 1970, unpublished.

[8] R. P. Huebener, "Superconductors in a temperature gradient," *Supercond. Sci. Technol.*, vol. 8, pp. 189–198, 1995.

[9] A. V. Ustinov, T. Doderer, R. P. Huebener, N. F. Pedersen, B. Mayer, and V. A. Oboznov, "Dynamics of sine-Gordon solitons in the annular Josephson junction," *Phys. Rev. Lett.*, vol. 69, pp. 1815–1818, 1992.

[10] S. Keil, R. Straub, R. Gerber, R. P. Huebener, D. Koelle, R. Gross, and K. Barthel, "Imaging of vortices and 1/f noise sources in YBCO dc SQUIDs using low-temperature scanning electron microscopy," *IEEE Trans. Appl. Supercond.*, vol. 9, no. 2, pp. 2961–2966, Jun. 1999.

[11] D. V. Abraimov, D. M. Feldmann, A. A. Polyanskii, A. Gurevich, S. Liao, G. Daniels, D. C. Larbalestier, A. P. Zhuravel, and A. V. Ustinov, "Imaging local dissipation and magnetic field in YBCO films with artificial defects," *IEEE Trans. Appl. Supercond.*, vol. 15, no. 2, pp. 2954–2957, Jun. 2005.